



# The feasibility of ultralow-activity $^{18}\text{F}$ -FDG dynamic PET imaging in lung adenocarcinoma patients through total-body PET/CT scanner

Jing Lv<sup>1,2,3</sup> · Hongyan Yin<sup>1,2,3</sup> · Haojun Yu<sup>1,2,3</sup> · Guobing Liu<sup>1,2,3</sup> · Hongcheng Shi<sup>1,2,3</sup>

Received: 12 March 2022 / Accepted: 3 July 2022 / Published online: 20 July 2022  
© The Author(s) under exclusive licence to The Japanese Society of Nuclear Medicine 2022

## Abstract

**Objective** To explore the feasibility of ultralow-activity  $^{18}\text{F}$ -FDG total-body dynamic PET imaging for clinical practice in patients with lung adenocarcinoma.

**Methods** Eight of 18 patients were randomly injected with  $^{18}\text{F}$ -FDG with full activity (3.7 MBq/kg) for total-body dynamic PET imaging, while 10 received one-tenth activity (0.37 MBq/kg). The generated time-to-activity curves (TACs) according to the regions of interest (ROIs) were processed by PMOD through standard FDG two-tissue compartment model fitting. The kinetic constant rates (K1, K2, K3, and Ki), radiation dose, prompt counts, and data storage size were analysed between the full- and ultralow-activity groups. The SUVmax-Tumour/SUVmax-Liver and SUVmax-Tumour/SUVmax-Muscle on static PET images were also assessed.

**Results** Each of the fitted models has a satisfactory goodness-of-fit with  $R^2$  greater than 0.9 except 3 (3/234) in ultralow-activity group, where one in pancreas ( $R^2=0.851$ ), another one in muscle ( $R^2=0.868$ ), and the third one in bone marrow ( $R^2=0.895$ ). All the fitted models in the full-activity group had a better goodness-of-fit than those in the ultralow-activity group. However, no significant differences were found in any of the kinetic metrics or image quality between the two groups except in the reduction of radiation dose and data storage size.

**Conclusions** The 10× reduction of injected  $^{18}\text{F}$ -FDG could achieve comparable kinetic metrics and T/N ratios by total-body dynamic PET imaging in lung adenocarcinoma patients. Ultralow-activity total-body PET imaging is feasible for clinical practice in oncological patients without obesity, especially in dynamic PET scanning.

**Keywords** Total-body dynamic PET imaging · 2-[ $^{18}\text{F}$ ]-fluoro-2-deoxy-D-glucose ( $^{18}\text{F}$ -FDG) · Ultralow-activity · Radiation dose · Lung adenocarcinoma

## Introduction

Positron emission tomography/computed tomography (PET/CT) with F-18-fluorodeoxyglucose ( $^{18}\text{F}$ -FDG) has been widely applied to the diagnosis, staging, restaging, and treatment efficacy evaluation of tumours [1–4]. Despite the potential value of providing both anatomical and functional

information for clinical decisions in oncological patients, radiation exposure remains a main concern for patients. Therefore, the demand for reducing the radiation dosimetry of PET/CT imaging without affecting the image quality has been increasing.

Recently, total-body PET/CT scanner, with a long axial field of view (AFOV) has ushered in the new era of PET/CT around the world. As we known, the Biograph Vision Quadra PET/CT LAFOV system (Siemens Healthineers, Knoxville, TN, USA) [5], the PennPET EXPLORER (built at the University of Pennsylvania) [6], and the uEXPLORER (United Imaging Healthcare, China) [7–9] have been successfully transitioned to clinical or research use. The uEXPLORER with a long AFOV up to 194 cm has been found to have a higher sensitivity by a factor of up to 40× theoretically and a better signal-to-noise ratio of more than a sixfold increase [10–13]. Due to the improved sensitivity, it allows

✉ Hongcheng Shi  
shi.hongcheng@zs-hospital.sh.cn

<sup>1</sup> Department of Nuclear Medicine, Zhongshan Hospital, Fudan University, 180 Fenglin Road, Shanghai 200032, China

<sup>2</sup> Nuclear Medicine Institute of Fudan University, Shanghai 200032, China

<sup>3</sup> Shanghai Institute of Medical Imaging, Shanghai 200032, China

for the reduced injected dose while maintaining the image quality in PET/CT imaging [10].

Considering the above advantages, our team has demonstrated that total-body PET/CT with a half-dose (1.85 MBq/kg)  $^{18}\text{F}$ -FDG activity can achieve comparable image quality to conventional PET/CT and even better than that of conventional PET/CT with routine clinical full-dose  $^{18}\text{F}$ -FDG in lung cancer [14]. In addition to the evaluation of static PET/CT imaging at a low injected dose, we also revealed that total-body dynamic PET imaging using a 10× reduction in injected activity could achieve relevant kinetic metrics of  $^{18}\text{F}$ -FDG and comparable image contrast with full-activity imaging in healthy volunteers [15].

However, the kinetic metrics of  $^{18}\text{F}$ -FDG in oncological patients did not exactly correspond to those in healthy volunteers due to the Warburg effect with a high ratio of anaerobic glycolysis in tumours [16]. It is even more important to evaluate whether there is a significant difference in kinetic metrics of  $^{18}\text{F}$ -FDG between ultralow-activity and full-activity in oncological patients, such as the  $^{18}\text{F}$ -FDG net uptake rate constant (Ki), which has been used in differentiating malignant from benign lung lesions [17] and metastatic lymph nodes [18]. Furthermore, Ki has also been proven to be more sensitive in detecting tumour response to cancer treatment [19, 20].

Thus, considering the previous paper on the evaluation of static PET/CT imaging in a low injected dose in patients with lung cancer, the aim of the present study was to investigate the feasibility of ultralow-activity  $^{18}\text{F}$ -FDG total-body PET/CT dynamic imaging for clinical practice in lung adenocarcinoma patients.

## Materials and methods

### Patients

This study was approved by the Institutional Review Board of Zhongshan Hospital, Fudan University, and conducted

after signing the written informed consent from each participant.

Fifteen of 35 patients who suspected lung cancer and underwent total-body dynamic PET/CT scanning were randomly selected for the full-activity group, whereas the remaining twenty were in the ultralow-activity group. Eight patients were eventually enrolled in the full-activity group, whereas ten were in the ultralow-activity group (Fig. 1). The missing patients were consisted of 10 undesired pathological results, 6 undesired body mass index (BMI), and 1 undesired other tumour history. The inclusion criteria were as follows: (1) no history of malignancy or organ excision before dynamic PET/CT scanning; (2) all patients were confirmed to have primary lung adenocarcinoma by postoperative pathological results after dynamic PET/CT scanning. The exclusion criteria were as follows: (1) distant organ or tissue metastasis on PET/CT findings; (2) a history of chronic disease such as diabetes, liver cirrhosis, renal/heart failure, hyperthyroidism, or hyperparathyroidism; (3) BMI ( $\text{kg}/\text{m}^2$ ) > 28.

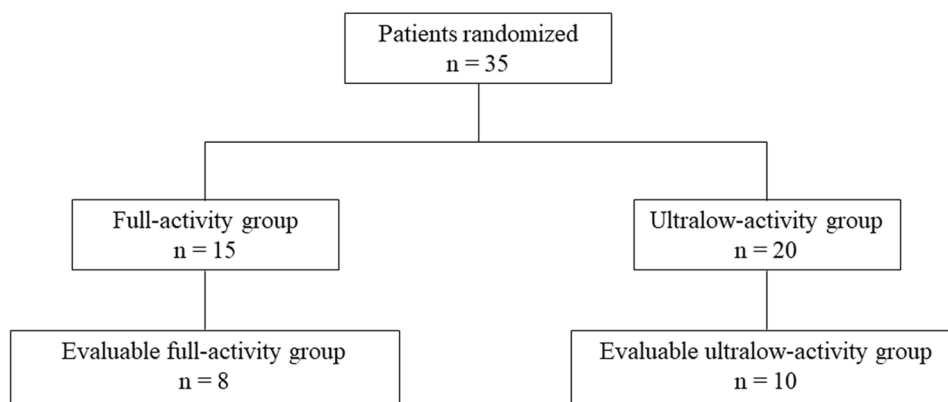
### Total-body dynamic PET/CT imaging

All patients were required to fast for 6 h prior to dynamic PET/CT imaging. Before the  $^{18}\text{F}$ -FDG injection, height, weight, and blood glucose level were measured and recorded on site. During dynamic PET imaging, patients were instructed to avoid speaking and moving.

A uEXPLORER PET/CT scanner (United Imaging Healthcare) was used for dynamic PET imaging. According to the guidelines of the European Association of Nuclear Medicine for  $^{18}\text{F}$ -FDG PET/CT oncological examination [1], an activity of  $4.1 \pm 0.33$  MBq/kg was injected in  $^{18}\text{F}$ -FDG full-activity patients, while  $0.41 \pm 0.03$  MBq/kg was injected in the ultralow-activity group. Then, 60 min dynamic PET scanning was started simultaneously with the injection of  $^{18}\text{F}$ -FDG in a vein near the ankle in all groups.

Before a diagnostic CT (tube current modulation of 120 kVp, spiral pitch factor of 0.9875, and slice thickness of

**Fig. 1** The flowchart of the randomly selected patients in full-activity group and ultralow-activity group



1 mm) in our scanning, a low-dose CT was performed first for attenuation correction (AC).

### Dynamic PET reconstruction

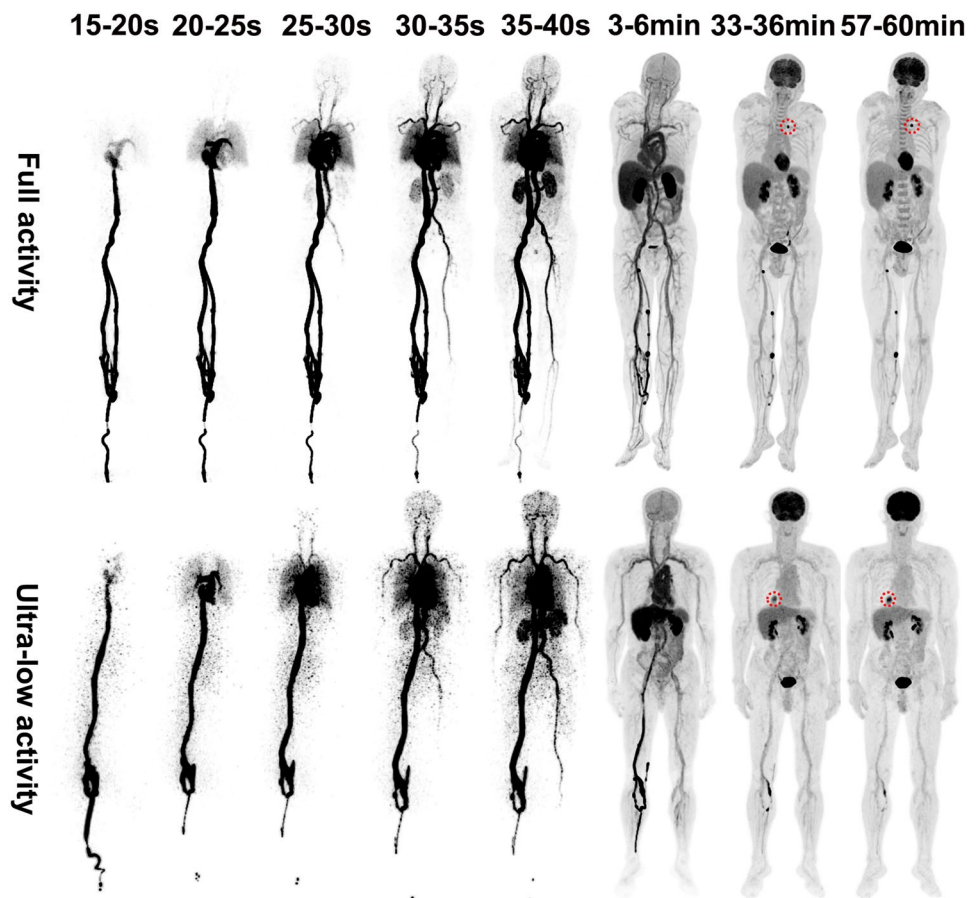
The PET images were reconstructed into a  $239 \times 239 \times 679$  matrix with voxels of  $2.85 \text{ mm}^3$  by the 3D list-mode OSEM algorithm, including high-resolution TOF and point-spread function modelling (OSEM–TOF–PSF) [21, 22]. For the dynamic PET image analysis, a series of PET images were divided into 55 frames with two kinds of schemes: a frame of 5 s for the initial 3 min ( $36 \times 5 \text{ s}$ ) and a frame of 3 min thereafter until the end ( $19 \times 180 \text{ s}$ ). Representative frames of PET images are shown in Fig. 2. Finally, the prompt events on PET images and total storage size were recorded.

### Generation of tissue activity curves (TACs)

A dedicated postprocessing workstation (uWS-MIR001, United Imaging Healthcare) with dynamic analysis software was used to process the reconstructed PET images and low-dose AC CT images. ROIs were drawn within 12 main organs and tumour lesions of the lung. Two-dimensional ROIs were placed on the target tissues instead of

three-dimensional ROIs to reduce the effect of unwanted areas beyond the boundary. For the tumour lesion, the freehand ROIs were placed on the solid components of the tumour to cover the largest tumour portion from the brightest slice of the PET image. For the blood pool, the ROI of the ascending aorta apart from the vessel wall was selected in this study, which was consistent with our previous studies [15, 23]. For the brain tissues, the ROIs were placed on the bilateral parietal cortex, white matter, cerebellum cortex, and medulla. For the liver, three ROIs apart from vessels were placed on the right lobe (upper, middle, and lower areas), and another one was placed on the middle of the left external lobe. For the spleen, the ROI was placed on the largest transaxial section. For the pancreas, the ROI was placed on the body area on the largest transaxial section. For the thyroid and kidney, the ROIs were placed on the middle areas of each side. For the muscle, bone marrow and bone, the ROIs were placed on the bilateral psoas major (on the same slice of PET image), bilateral medullary cavities in the upper areas of the femurs (on the same slice of PET image), and the third lumbar body, respectively. Finally, TACs were extracted from the above ROIs including lung tumour lesions.

**Fig. 2** Maximum-intensity projections of selected dynamic reconstructed images from a patient in the full-activity group (upper row) and the ultralow-activity group (lower row). Red dotted circles were placed on the tumour lesions



## Mathematic model fitting and parameter generation

PMOD Kinetic Modelling (Version 3.2, Zürich, Switzerland), independent of the built-in workstation, was used to process the complete TAC data through the standard FDG two-tissue compartment model fitting. In each model fitting, the data of the ascending aorta were chosen for the temporal whole-blood activity ( $CB(t)$ ). In addition,  $CB(t)$  was corrected according to a previous study [24] to estimate the plasma input function ( $CP(t)$ ), where the haematocrit was different by sex (0.42 for men and 0.36 for women), and the equilibration time constant was  $0.2346 \text{ min}^{-1}$ . The kinetic rate constants (Fig. 3) including K1 (the transport of  $^{18}\text{F}$ -FDG forward from plasma to tissues), K2 (the transport of  $^{18}\text{F}$ -FDG backward from plasma to tissues), K3 (the intracellular  $^{18}\text{F}$ -FDG phosphorylation), K4 (the intracellular  $^{18}\text{F}$ -FDG dephosphorylation), and the fraction of blood volume in tissue ( $\nu_B$ ) codetermined the temporal tissue activity of  $^{18}\text{F}$ -FDG ( $CPET(t)$ ), including  $CB(t)$  for spillover correction and  $CP(t)$  for input curve. Finally, the  $K_i$  was calculated through the following equation:

$$K_i = \frac{K_1 * K_3}{K_2 + K_3}$$

In addition, the evaluation of goodness-of-fit in each model fitting was through the recorded Akaike information criterion (AIC) [25, 26], the Schwarz criterion (SC) [27], and the determination index ( $R^2$ ). Representative model fittings are shown in Fig. 4.

## Statistical analysis

All data are presented as the mean  $\pm$  standard deviation (SD), including median and Coefficient of Variation (CoV%)

if necessary. The statistical software SPSS 17 (IBM SPSS Inc., Chicago, Illinois, USA) and GraphPad Prism 5 software (GraphPad Software, San Diego, CA, USA) were used to perform statistical analyses. The chi-squared test and Fisher's exact test were performed for comparisons of categorical variables, while Student's  $t$  test or the Mann–Whitney  $U$  test was used for continuous variables depending on the Kolmogorov–Smirnov test. A  $p$  value less than 0.05 for the two sides was considered statistically significant.

## Results

### The general patient characteristics

The general patient characteristics are shown in Table 1. There was no significant difference between the full-activity and ultralow-activity groups in age, sex, height, weight, BMI, blood glucose, tumour pathological grade, tumour long diameter or SUVmax of the tumour lesion, except for the core variable of injected  $^{18}\text{F}$ -FDG activity ( $p < 0.001$ ).

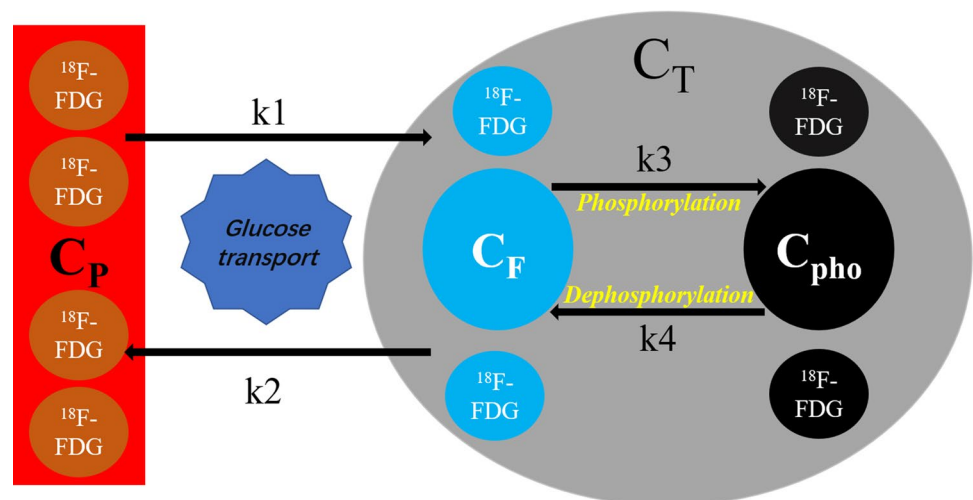
### Kinetic metrics of $^{18}\text{F}$ -FDG between the full-activity and ultralow-activity groups

The kinetic constant rates K1, K2, K3, and  $K_i$  of  $^{18}\text{F}$ -FDG in normal organs as well as lung tumours are shown in Table 2 and Table 3. No significant differences in the above kinetic constant rates in measured tissues were found between the full-activity and ultralow-activity groups.

### The goodness-of-fit of model fitting

Each of the fitted models had a satisfactory goodness-of-fit with  $R^2$  greater than 0.9 except 3 (3/234) fitted models with  $R^2$  less than 0.9 (Table 4). All the above 3 fitted

**Fig. 3** The schematic of two-tissue compartment models



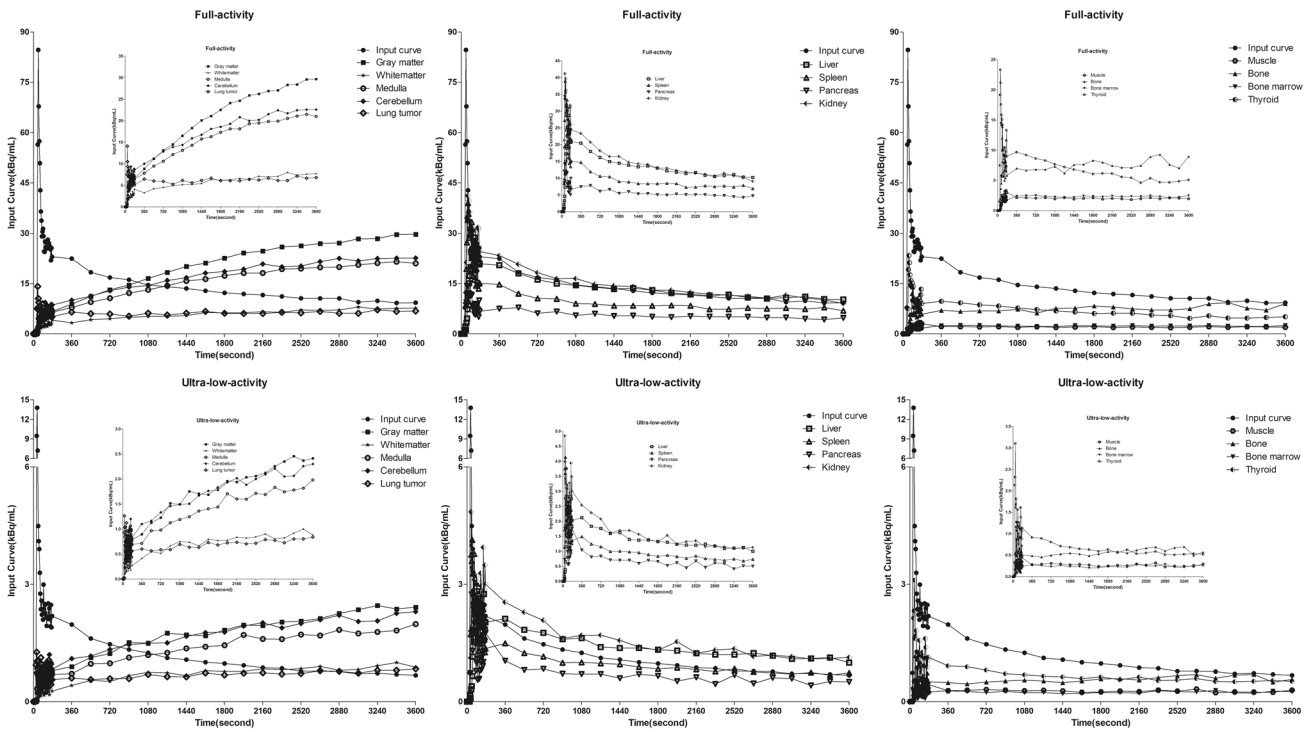


**Fig. 4** Time courses and model fitting of <sup>18</sup>F-FDG with original data in normal organs and tumour lesions in a representative patient from the full-activity group (upper row) and the ultra-low-activity group (lower row)

**Table 1** General patient characteristics

Variables	Full-activity	Ultra-low-activity	<i>P</i> value
<i>N</i>	8	10	
Age, years			0.69
Mean ± SD	60.6 ± 5.7	59.0 ± 9.2	
Range	50–67	42–68	
Gender			0.64
Male	5	4	
Female	3	6	
Height (cm)	165.6 ± 8.9	162.8 ± 8.2	0.53
Weight (kg)	65.2 ± 8.5	60.6 ± 13.8	0.44
BMI (kg/m <sup>2</sup> )	23.8 ± 2.5	22.5 ± 3.2	0.40
Blood glucose (mmol/l)	5.0 ± 0.6	5.8 ± 0.7	0.27
Injected dose (MBq)	251.4 ± 35.0	23.6 ± 5.25	<0.001
Injected dose/weight (MBq/kg)	3.9 ± 0.3	0.4 ± 0.03	<0.001
Pathological grade			0.88
Well-differentiated (<II)	3	2	
Poorly differentiated (>II)	5	7	
Tumour long diameter	23.5 ± 6.8	26.7 ± 9.7	0.47
SUVmax	6.9 ± 4.2	13.2 ± 10.2	0.14

models were in ultra-low-activity group, where one in pancreas ( $R^2 = 0.851$ ), another one in muscle ( $R^2 = 0.868$ ), and the third one in bone marrow ( $R^2 = 0.895$ ). In addition, all the fitted models in the full-activity group had relatively

smaller AICs and SC, as well as larger  $R^2$  values than the ultra-low-activity group, with a significant difference in some of the measured organs.

**Table 2** Summary of kinetic metrics (K1 and K2) between full-activity and ultra-low-activity groups

Organs	K1 (min <sup>-1</sup> )			K2 (min <sup>-1</sup> )		
	Full-activity	Ultra-low-activity	<i>P</i> value	Full-activity	Ultra-low-activity	<i>P</i> value
	Mean ± SD	Mean ± SD		Mean ± SD	Mean ± SD	
Grey matter	0.097 ± 0.019	0.101 ± 0.019	0.710	0.075 ± 0.024	0.098 ± 0.049	0.0.250
White matter	0.047 ± 0.006	0.045 ± 0.006	0.514	0.119 ± 0.026	0.096 ± 0.025	0.00.102
Medulla	0.094 ± 0.018	0.092 ± 0.012	0.740	0.152 ± 0.100	0.142 ± 0.041	0.797
Cerebellum	0.128 ± 0.017	0.136 ± 0.018	0.412	0.131 ± 0.020	0.154 ± 0.044	0.217
Thyroid	0.700 ± 0.574	0.626 ± 0.306	0.745	2.111 ± 1.661	1.805 ± 0.981	0.652
Lung tumour	0.118 ± 0.076	0.215 ± 0.128	0.094	0.477 ± 0.529	0.849 ± 0.628	0.226
Liver	0.411 ± 0.068	0.526 ± 0.177	0.120	0.430 ± 0.072	0.496 ± 0.170	0.341
Spleen	1.254 ± 0.330	1.181 ± 0.435	0.716	2.259 ± 0.884	1.859 ± 0.467	0.262
Pancreas	0.491 ± 0.338	0.578 ± 0.307	0.598	1.642 ± 0.905	1.513 ± 0.967	0.788
Kidney	0.820 ± 0.235	0.771 ± 0.159	0.625	0.996 ± 0.333	0.772 ± 0.227	0.130
Muscle	0.053 ± 0.024	0.101 ± 0.057	0.052	0.415 ± 0.139	0.751 ± 0.541	0.126
Bone	0.125 ± 0.014	0.159 ± 0.068	0.206	0.522 ± 0.148	0.517 ± 0.236	0.959
Bone marrow	0.034 ± 0.011	0.029 ± 0.012	0.407	0.281 ± 0.083	0.266 ± 0.079	0.711

**Table 3** Summary of kinetic metrics (K3 and Ki) between full-activity and ultra-low-activity groups

Organs	K3 (min <sup>-1</sup> )			Ki (min <sup>-1</sup> )		
	Full-activity	Ultra-low-activity	<i>P</i> value	Full-activity	Ultra-low-activity	<i>P</i> value
	Mean ± SD	Mean ± SD		Mean ± SD	Mean ± SD	
Grey matter	0.069 ± 0.017	0.046 ± 0.019	0.710	0.037 ± 0.008	0.032 ± 0.005	0.151
White matter	0.071 ± 0.014	0.031 ± 0.008	0.514	0.009 ± 0.002	0.011 ± 0.002	0.086
Medulla	0.079 ± 0.028	0.056 ± 0.021	0.740	0.024 ± 0.005	0.026 ± 0.006	0.531
Cerebellum	0.089 ± 0.022	0.047 ± 0.015	0.412	0.032 ± 0.005	0.032 ± 0.006	0.956
Thyroid	0.024 ± 0.009	0.014 ± 0.005	0.745	0.005 ± 0.002	0.005 ± 0.001	0.835
Lung tumour	0.114 ± 0.391	0.127 ± 0.054	0.094	0.024 ± 0.014	0.031 ± 0.015	0.362
Liver	0.008 ± 0.001	0.003 ± 0.001	0.120	0.003 ± 0.001	0.004 ± 0.001	0.326
Spleen	0.012 ± 0.002	0.008 ± 0.003	0.716	0.004 ± 0.001	0.005 ± 0.001	0.066
Pancreas	0.019 ± 0.007	0.011 ± 0.005	0.598	0.005 ± 0.002	0.004 ± 0.002	0.519
Kidney	0.008 ± 0.003	0.006 ± 0.003	0.625	0.004 ± 0.002	0.006 ± 0.002	0.054
Muscle	0.036 ± 0.008	0.017 ± 0.007	0.052	0.002 ± 0.0005	0.002 ± 0.001	0.230
Bone	0.056 ± 0.010	0.030 ± 0.009	0.206	0.008 ± 0.002	0.009 ± 0.003	0.423
Bone marrow	0.029 ± 0.007	0.011 ± 0.003	0.407	0.002 ± 0.001	0.001 ± 0.001	0.299

### Comparisons of Ki, SUVmax, and T/N ratio in lung tumour lesions

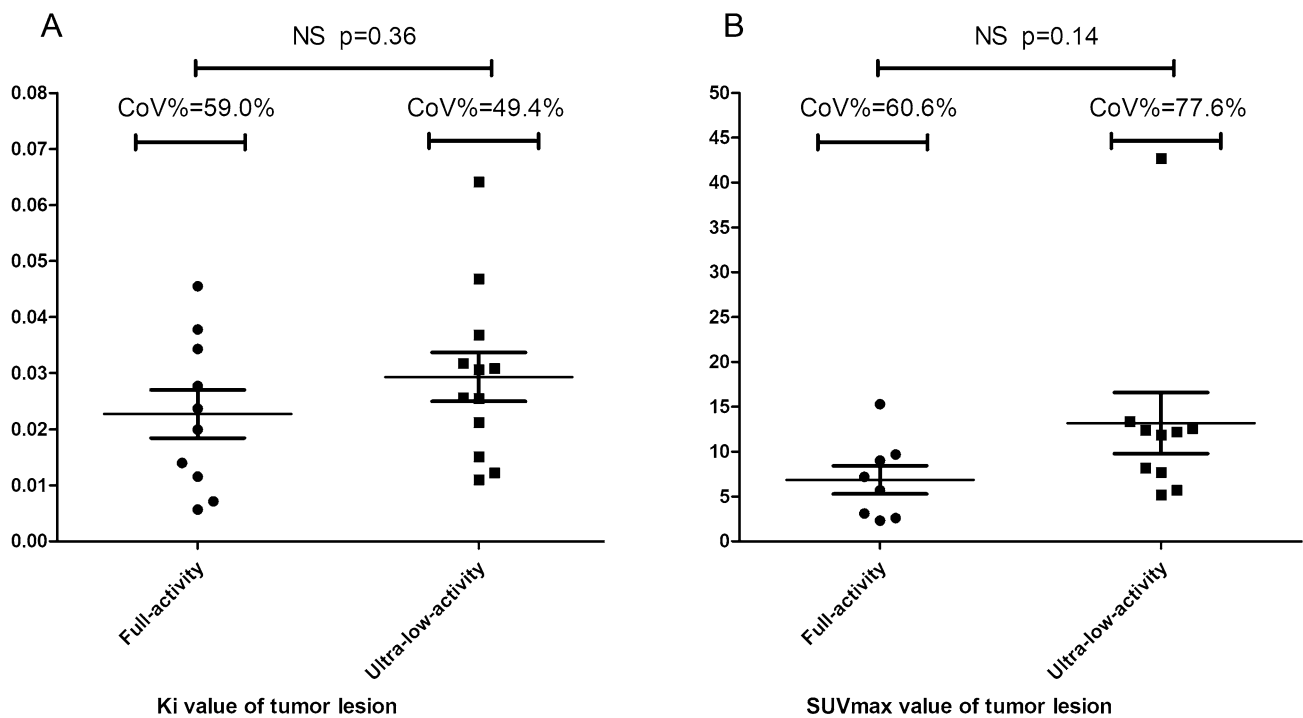
The Ki in tumour lesions was not significantly different between the full-activity and ultralow-activity groups, nor was the SUVmax of the tumour (Fig. 5). However, the CoV% of SUVmax was higher than Ki in both groups. In addition, the SUVmax-Tumour/SUVmax-Liver (Median 1.58, range 0.66–3.05 vs. Median 1.84, range 0.84–4.45) as well as SUVmax-Tumour/SUVmax-Muscle (Median 8.11, range 2.69–17.41 vs. Median 8.01, range 2.85–19.81) were also not significantly different between full-activity and ultra-low-activity group (Fig. 6).

### Comparisons of prompt events and storage size

The prompt counts from PET data, including the true, scatter, and random counts, were larger in the full-activity group than in the ultralow-activity group. Furthermore, the effective counts in each frame were also larger in the full-activity group. (Table 5).

**Table 4** The evaluation of goodness-of-fit in PMOD kinetic model fitting

Organs	AIC (Mean ± SD)			SC (Mean ± SD)			R <sup>2</sup> (Mean ± SD)		
	Full-activity	Ultra-low-activity	P value	Full-activity	Ultra-low-activity	P value	Full-activity	Ultra-low-activity	P value
Grey matter	37.5 ± 23.4	94.1 ± 14.8	< 0.001	45.5 ± 23.4	101.9 ± 14.8	< 0.001	0.994 ± 0.003	0.980 ± 0.009	< 0.001
White matter	38.1 ± 20.4	107.7 ± 13.9	< 0.001	44.8 ± 20.6	115.3 ± 14.0	< 0.001	0.990 ± 0.005	0.961 ± 0.008	< 0.001
Medulla	56.7 ± 19.8	108.6 ± 19.4	< 0.001	64.7 ± 19.8	116.5 ± 19.5	< 0.001	0.988 ± 0.007	0.968 ± 0.011	< 0.001
Cerebellum	51.9 ± 15.7	108.2 ± 12.7	< 0.001	60.0 ± 15.7	116.2 ± 12.7	< 0.001	0.990 ± 0.004	0.967 ± 0.011	< 0.001
Thyroid	42.9 ± 18.3	85.7 ± 29.5	0.003	48.3 ± 18.5	91.7 ± 29.8	0.003	0.968 ± 0.015	0.927 ± 0.022	< 0.001
Lung tumour	43.0 ± 24.1	62.7 ± 25.7	0.136	50.2 ± 24.2	64.0 ± 26.2	0.147	0.970 ± 0.023	0.968 ± 0.020	0.869
Liver	89.8 ± 16.8	95.5 ± 14.7	0.485	96.4 ± 17.4	101.6 ± 15.3	0.538	0.936 ± 0.019	0.916 ± 0.017	0.039
Spleen	102.9 ± 17.7	95.6 ± 20.4	0.459	109.8 ± 18.2	101.8 ± 21.1	0.439	0.930 ± 0.020	0.925 ± 0.018	0.558
Pancreas	98.7 ± 22.9	75.3 ± 22.3	0.055	105.0 ± 23.7	80.0 ± 23.1	0.049	0.919 ± 0.009	0.911 ± 0.026	0.471
Kidney	50.5 ± 18.4	83.0 ± 19.2	0.003	55.6 ± 19.3	89.0 ± 19.9	0.003	0.968 ± 0.014	0.933 ± 0.017	< 0.001
Muscle	96.7 ± 26.1	69.3 ± 21.6	0.036	103.5 ± 26.6	74.1 ± 22.0	0.027	0.936 ± 0.014	0.917 ± 0.023	0.075
Bone	94.7 ± 18.5	74.9 ± 23.0	0.081	101.7 ± 19.4	79.9 ± 23.9	0.067	0.935 ± 0.021	0.918 ± 0.010	0.052
Bone marrow	113.8 ± 26.8	84.7 ± 21.6	0.029	120.8 ± 27.5	90.1 ± 22.2	0.025	0.927 ± 0.016	0.920 ± 0.014	0.343

**Fig. 5** Comparisons of Ki and SUVmax in tumour lesions between the full-activity group and the ultralow-activity group

## Discussion

To our knowledge, the present study was the first to explore the difference in <sup>18</sup>F-FDG kinetic constant rates between full-activity and ultralow-activity lung adenocarcinoma patients through total-body dynamic PET imaging. Despite one tenth of the injected dose, the kinetic constant

rates in ultralow activity were not significantly different from those in full activity.

In our previous research [15], we demonstrated that ultralow-activity total-body dynamic PET imaging allows equal performance to full-activity PET imaging for investigating kinetic metrics of <sup>18</sup>F-FDG in healthy volunteers. Oncological patients, however, were the biggest beneficiary group when performing PET/CT imaging rather than healthy

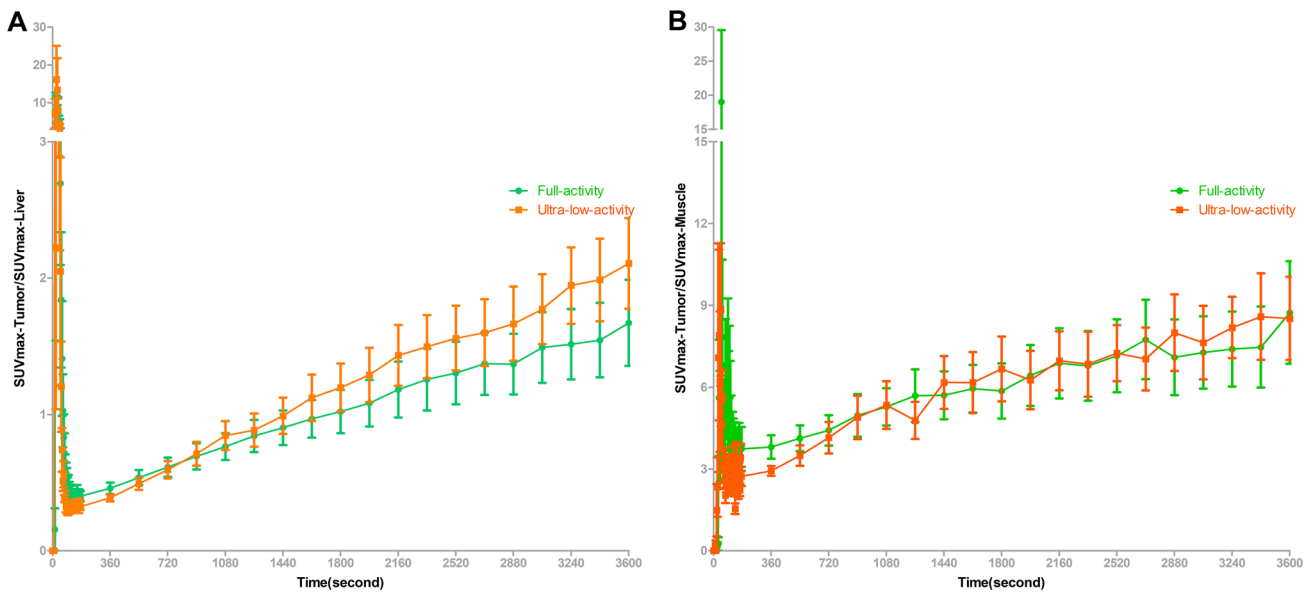


**Fig. 6** The SUVmax-Tumour/SUVmax-Liver and SUVmax-Tumour/SUVmax-Muscle on the PET image between the full-activity group and the ultralow-activity group. No significant difference was found between the two groups

**Table 5** The difference of prompt count, data storage, reconstruction time, and radiation dosimetry between full-activity and ultra-low-activity group

Variable	Group	
	Full-activity	Ultra-low-activity
Total counts(billion)	47.74 (34.38–115.45)	3.38 (2.92–4.39)
Prompt counts	41.98 (29.74–106.63)	2.77 (2.38–3.53)
Random counts	25.81 (16.49–75.60)	1.04 (0.86–1.37)
True counts	16.17 (13.25–31.03)	1.73 (1.55–2.23)
Scatter counts	5.65 (4.64–8.82)	0.61 (0.50–0.86)
Noise equal counts	2.48 (2.03–4.62)	0.46 (0.43–0.54)
Effective counts (Ture + Scatter)	21.82 (17.89–39.96)	2.34 (2.05–3.10)
Effective counts/frame (million)	396.73 (324.00–720.00)	42.54 (36.00–57.60)
Data storage (GByte)	631.0 (439.0–774.0)	63.6 (57.3–101.0)

volunteers. In addition, the presence of tumours may affect the  $^{18}\text{F}$ -FDG metabolism of other organs. Therefore, it is meaningful to further evaluate the  $^{18}\text{F}$ -FDG kinetic constant rates in oncological patients between different injected dose groups by the total-body PET scanner.

Due to the high sensitivity of the total-body PET/CT scanner, we successfully decreased the injected  $^{18}\text{F}$ -FDG dose up to one tenth of the common dose again for dynamic PET imaging. Two-dimensional ROIs were preferred in our study instead of three-dimensional ROIs to avoid unwanted areas beyond the target organ. Despite the ultralow injected dose, no significant differences in the Ki or SUVmax in tumour lesions were found when compared to the full-activity group. Moreover, the Ki of lung adenocarcinoma in our study was similar to Yang's study [18] despite the Patlak graphic analysis in their study. However, the Ki of lung adenocarcinoma was obviously lower than that of lung

squamous cell carcinoma (SCC) in Yang's paper. This was in line with the fact that SCC displayed more FDG uptake than lung adenocarcinoma [28].

In our study, both the Ki and the SUVmax of tumour in the ultralow-activity group were higher than the full-activity group despite of no statistical difference, due to the higher proportion of the patients with poorly differentiated cancer in ultralow-activity group. However, the CoV% of SUVmax was higher than Ki in both groups, which indicated that the SUVmax was more susceptible to interference. Furthermore, the SUVmax-Tumour/SUVmax-Liver and SUVmax-Tumour/SUVmax-Muscle were also not significantly different between the two groups, which indicated that the static image quality in the ultralow-activity group was equal to that in the full-activity group. In addition to the tumour lesion, the Ki in other measured tissues was also not significantly different between the full-activity and ultralow-activity



groups. Therefore, considering another study [14] from our team about half-dose  $^{18}\text{F}$ -FDG compared with conventional PET/CT using full-dose FDG in lung cancer, we have strongly demonstrated the feasibility of low-activity both in static and dynamic PET/CT scanning by total-body PET/CT in lung cancer patients.

The tenfold reduction in injected  $^{18}\text{F}$ -FDG dose is a huge attractive advantage of decreasing radiation exposure. However, research on low-activity PET/CT scanning is rare due to the intrinsically noisy nature of PET modalities, especially dynamic PET scanning. Furthermore, the low signal-to-noise ratio (SNR) of dynamic PET data is a major obstacle which can cause the severe deviation in the evaluation of dynamic parameter [29]. To achieve equivalent image quality and lesion detectability when compared with full activity, the lowest PET counts need to reach 5 million in low-activity scanning [30]. In our study, the median effective count in each frame was 42.54 million in the ultralow-activity group, which exceeded the minimum requirement described above. Despite no denoising method in our dynamic study while the nonlocal means (NLM) method in Wu's study [31], the random counts and noise equal counts (NEC) were also decreased in ultralow-activity compared with full activity, which may improve the image quality despite the lower total counts.

In addition to the advantage of decreasing radiation exposure, the lower storage of PET/CT scanning data in ultralow activity, especially in dynamic scanning, is another attractive point that relieves the burden of storage in clinical workstations. The median size of the data in the full-activity group was more than 631 GB, while it was 63.6 GB in ultra-low-activity group. The nearly tenfold reduction in data size offered the huge possibility to store more research data in the limited storage capacity of clinical workstations.

Despite the advantages in the ultralow-activity group described above, we found that the goodness-of-fit of model fitting in the full-activity group was superior to that in the ultralow-activity group, which indicated that a sufficient injected dose of  $^{18}\text{F}$ -FDG was required for dynamic PET imaging to guarantee stable model fitting. This reason also applied to the diverse goodness-of-fit in different organs, which explained that organs with high  $^{18}\text{F}$ -FDG metabolism, such as brain tissues, showed better model fitting, whereas those with low  $^{18}\text{F}$ -FDG metabolism, such as pancreas, muscle, and bone marrow, showed relatively poor model fitting with  $R^2$  less than 0.9. Furthermore, this may offer the reasonable explanation of the  $p$  value is more than but near the 0.05 in  $K_1$  value in muscle as well as  $K_3$  value. Due to the high  $^{18}\text{F}$ -FDG metabolism in tumours, the tumour lesion also displayed better model fitting than other organs except brain tissues, even in the ultralow-activity group.

However, there are still several unavoidable limitations in this study. First, the interclass variances of kinetic constants

in some organs, especially for organs with low  $^{18}\text{F}$ -FDG metabolism, were still substantial in both the ultralow-activity and full-activity groups. Second, the patients in each group were not large enough and lacked a portion of advanced metastatic lung adenocarcinoma. Hence, a follow-up study on dynamic PET scanning may recruit more patients to avoid similar limitations. Third, the dynamic PET imaging with 60 min is too long for the clinical practice and too difficult for the oncological patients to avoid slight movement. For this reason, the short time dynamic PET imaging may be more attractive in the future.

## Conclusion

We demonstrated that there were no significant differences in kinetic metrics or image quality after one-tenth injected dose of  $^{18}\text{F}$ -FDG using a high-sensitivity total-body PET scanner in lung adenocarcinoma patients compared to full-activity dynamic imaging, except in the reduction of radiation dose and data storage size. Thus, combined with our previous work related to the decreased injected dose of  $^{18}\text{F}$ -FDG by a total-body PET scanner, it is feasible to use one-tenth injected dose of  $^{18}\text{F}$ -FDG for clinical practice in oncological patients without obesity in dynamic PET scanning.

**Funding** This study is supported by Shanghai Municipal Key Clinical Specialty Project (shslczdk03401), Clinical Research Plan of SHDC (SHDC2020CR3079B), Science and Technology Committee of Shanghai Municipality(20DZ2201800), Special Fund for Clinical Research of Zhongshan Hospital, Fudan University(2020ZSLC63), The Youth Medical Talents-Medical Imaging Practitioner Program of Shanghai "Rising Stars of Medical Talent" Youth Development Program (SHWRS [2020]087), The National Natural Science Foundation of China (82001863), and the Shanghai Sailing Program (19YF1408200).

## Declarations

**Conflict of interest** The authors declare that there is no conflict of interests.

## References

1. Boellaard R, Delgado-Bolton R, Oyen WJ, et al. FDG PET/CT: EANM procedure guidelines for tumour imaging: version 2.0. *Eur J Nucl Med Mol Imaging*. 2015;42(2):328–54.
2. Fletcher JW, Djulbegovic B, Soares HP, et al. Recommendations on the use of  $^{18}\text{F}$ -FDG PET in oncology. *J Nucl Med*. 2008;49(3):480–508.
3. Bosch KD, Chicklore S, Cook GJ, et al. Staging FDG PET-CT changes management in patients with gastric adenocarcinoma who are eligible for radical treatment. *Eur J Nucl Med Mol Imaging*. 2020;47(4):759–67.
4. Broccoli A, Nanni C, Cappelli A, et al. Diagnostic accuracy of positron emission tomography/computed tomography-driven

- biopsy for the diagnosis of lymphoma. *Eur J Nucl Med Mol Imaging*. 2020;47(13):3058–65.
5. Alberts I, Hunermond JN, Prenosil G, et al. Clinical performance of long axial field of view PET/CT: a head-to-head intra-individual comparison of the biograph vision quadra with the biograph vision PET/CT. *Eur J Nucl Med Mol Imaging*. 2021;48(8):2395–404.
  6. Viswanath V, Daube Witherspoon ME, Karp JS, et al. Numerical observer study of lesion detectability for a long axial field-of-view whole-body PET imager using the PennPET explorer. *Phys Med Biol*. 2020;65(3): 035002.
  7. Xiao J, Yu H, Sui X, et al. Can the BMI-based dose regimen be used to reduce injection activity and to obtain a constant image quality in oncological patients by (18)F-FDG total-body PET/CT imaging? *Eur J Nucl Med Mol Imaging*. 2021;49(1):269–78.
  8. Hu P, Zhang Y, Yu H, et al. Total-body (18)F-FDG PET/CT scan in oncology patients: how fast could it be? *Eur J Nucl Med Mol Imaging*. 2021;48(8):2384–94.
  9. Zhang Y, Hu P, Wu R, et al. The image quality, lesion detectability, and acquisition time of (18)F-FDG total-body PET/CT in oncological patients. *Eur J Nucl Med Mol Imaging*. 2020;47(11):2507–15.
  10. Cherry SR, Jones T, Karp JS, et al. Total-body PET: maximizing sensitivity to create new opportunities for clinical research and patient care. *J Nucl Med*. 2018;59(1):3–12.
  11. Zhang X, Badawi RD, Cherry SR, et al. Theoretical study of the benefit of long axial field-of-view PET on region of interest quantification. *Phys Med Biol*. 2018;63(13):135010.
  12. Cherry SR, Badawi RD, Karp JS, et al. Total-body imaging: transforming the role of positron emission tomography. *Sci Transl Med*. 2017;9(381):eaaf6169.
  13. Surti S, Karp JS. Impact of detector design on imaging performance of a long axial field-of-view, whole-body PET scanner. *Phys Med Biol*. 2015;60(13):5343–58.
  14. Tan H, Sui X, Yin H, et al. Total-body PET/CT using half-dose FDG and compared with conventional PET/CT using full-dose FDG in lung cancer. *Eur J Nucl Med Mol Imaging*. 2021;48(6):1966–75.
  15. Liu G, Hu P, Yu H, et al. Ultra-low-activity total-body dynamic PET imaging allows equal performance to full-activity PET imaging for investigating kinetic metrics of (18)F-FDG in healthy volunteers. *Eur J Nucl Med Mol Imaging*. 2021;48(8):2373–83.
  16. Warburg O, Wind F, Negelein E. The metabolism of tumors in the body. *J Gen Physiol*. 1927;8(6):519–30.
  17. Gupta N, Gill H, Graeber G, et al. Dynamic positron emission tomography with F-18 fluorodeoxyglucose imaging in differentiation of benign from malignant lung/mediastinal lesions. *Chest*. 1998;114(4):1105–11.
  18. Yang M, Lin Z, Xu Z, et al. Influx rate constant of (18)F-FDG increases in metastatic lymph nodes of non-small cell lung cancer patients. *Eur J Nucl Med Mol Imaging*. 2020;47(5):1198–208.
  19. Romer W, Hanauske AR, Ziegler S, et al. Positron emission tomography in non-Hodgkin's lymphoma: assessment of chemotherapy with fluorodeoxyglucose. *Blood*. 1998;91(12):4464–71.
  20. Wahl RL, Zasadny K, Helvie M, et al. Metabolic monitoring of breast cancer chemohormonotherapy using positron emission tomography: initial evaluation. *J Clin Oncol*. 1993;11(11):2101–11.
  21. Zhang X, Xie Z, Berg E, et al. Total-body dynamic reconstruction and parametric imaging on the uEXPLORER. *J Nucl Med*. 2020;61(2):285–91.
  22. Zhang X, Zhou J, Cherry SR, et al. Quantitative image reconstruction for total-body PET imaging using the 2-meter long EXPLORER scanner. *Phys Med Biol*. 2017;62(6):2465–85.
  23. Liu G, Xu H, Hu P, et al. Kinetic metrics of (18)F-FDG in normal human organs identified by systematic dynamic total-body positron emission tomography. *Eur J Nucl Med Mol Imaging*. 2021;48(8):2363–72.
  24. Wahl LM, Asselin MC, Nahmias C. Regions of interest in the venous sinuses as input functions for quantitative PET. *J Nucl Med*. 1999;40(10):1666–75.
  25. Akaike H. A new look at the statistical model identification. *IEEE Trans Automat Contr*. 1974;19:716–23.
  26. Akaike H. An information criterion (AIC). *Math Sci*. 1976;14:5–9.
  27. Schwarz G. Estimating the dimension of a model. *Ann Stat*. 1978;6(2):461–4.
  28. de Geus-Oei LF, van Krieken JH, Aliredjo RP, et al. Biological correlates of FDG uptake in non-small cell lung cancer. *Lung Cancer*. 2007;55(1):79–87.
  29. Kimura Y, Naganawa M, Shidahara M, et al. PET kinetic analysis –pitfalls and a solution for the Logan plot. *Ann Nucl Med*. 2007;21(1):1–8.
  30. Schaefferkoetter JD, Yan J, Townsend DW, et al. Initial assessment of image quality for low-dose PET: evaluation of lesion detectability. *Phys Med Biol*. 2015;60(14):5543–56.
  31. Wu Y, Feng T, Shen Y, et al. Total-body parametric imaging using the Patlak model: feasibility of reduced scan time. *Med Phys*. 2022;49(7):4529–39.

**Publisher's Note** Springer Nature remains neutral with regard to jurisdictional claims in published maps and institutional affiliations.